Across-track Extension of Retrieved Cloud and Aerosol Properties for the EarthCARE Mission: The ACM-3D Product

ZHIPENG QU

Environment and Climate Change Canada, Toronto, ON, Canada

HOWARD W. BARKER*

Environment and Climate Change Canada, Victoria, BC, Canada

JASON N. S. COLE   MARK W. SHEPHARD

Environment and Climate Change Canada, Toronto, ON, Canada

Submitted: 1 November 2022

Revised: xx xxxx xxxx

For publication in: *Atmos. Meas. Tech.*

____

* Corresponding author address: Howard Barker; howard.barker@ec.gc.ca

Abstract

The narrow cross-section of cloud and aerosol properties retrieved by L2-algorithms that operate on data from EarthCARE's nadir-pointing sensors gets "broadened" across-track by an algorithm that is described and demonstrated here. This *Scene Construction Algorithm* (SCA) consists of four components. At its core is a radiance-matching procedure that works with measurements made by EarthCARE's Multi-Spectral Imager (MSI). In essence, an off-nadir pixel gets filled with retrieved profiles that are associated with a (nearby) nadir pixel whose MSI radiances best match those of the off-nadir pixel. The SCA constructs a 3D array of cloud and aerosol (and surface) properties for entire *frames* that measure ~6,000 km along-track by 150 km across-track (i.e., the MSI's full swath). Constructed domains out to ~15 km across-track on both sides of nadir are used explicitly downstream as input for 3D radiative transfer models that predict top-of-atmosphere (TOA) broadband solar and thermal fluxes and radiances. These quantities are compared to commensurate measurements made by EarthCARE's BroadBand Radiometer (BBR), thus facilitating a continuous closure assessment of the retrievals. Three 6,000 km x 200 km frames of synthetic EarthCARE observations were used to demonstrate the SCA. The main conclusion is that errors in modelled TOA fluxes that stem from use of 3D domains produced by the SCA are expected to be less than ±5 W m^{-2} and rarely larger than ±10 W m^{-2}. As such, the SCA, as purveyor of information needed to run 3D radiative transfer models, should help more than hinder the radiative closure assessment of EarthCARE's L2 retrievals.

1. Introduction

The objective of the EarthCARE satellite mission is to help improve numerical predictions of weather, air quality, and climatic change via application of synergistic L2-retrieval algorithms to observational data from its cloud-profiling radar (CPR), backscattering lidar (ATLID), and passive multi-spectral imager (MSI) (Illingworth et al. 2015). EarthCARE's overarching scientific goal (ESA 2001) is to retrieve cloud and aerosol properties with enough accuracy that when used to initialize atmospheric radiative transfer (RT) models, simulated top-of-atmosphere (TOA) broad-band radiative fluxes, for domains covering ~100 km^2, agree with their observational-based coun-terparts to within ± 10 W m^{-2} *more often than not*. "Observed" TOA fluxes derive from radiances measured by EarthCARE's multi-angle broadband radiometer (BBR). As the latter are not used by retrieval algorithms, comparing them to modelled values, obtained by RT models operating on retrieved quantities, affects a "moderately stringent" verification of the retrievals (Barker et al. 2023); "moderately stringent" because BBR radiances consist, in part, of photons that share the same gaseous pathlength and number of cloud-aerosol-surface scattering event distributions as those that constitute MSI radiances. These imperfections aside, this radiative closure verification is a well-defined and cost-effective final stage in EarthCARE's formal processing chain (Eisinger et al. 2023).

In light of EarthCARE's ambitious goal of limiting differences between measured and modelled TOA fluxes to ± 10 W m^{-2} when averaged over "assessment domains" that measure ~5 km across-track by ~21 km along-track, the usefulness of its radiative closure programme depends much on reducing errors and uncertainties in: BBR measurements; variables needed by RT models that are not provided by EarthCARE observations; and RT models. Included in this are issues of observa-tional geometry that face use of BBR data for EarthCARE's closure assessment. First, L2-retrieved

77   profiles are ~1 km in diameter, while the BBR was designed to perform best for footprints of ~10

78   x 10 km. For this configuration, fluxes and radiances computed for sequences of retrieved profiles

79   contribute only ~10% of the signal to each BBR footprint (or pixel). Second, at only ~1 km wide,

80   net horizontal fluxes for each retrieved column, and sequences of them, will rarely be close to zero

81   (e.g., Barker and Li 1997; Marshak et al. 1998). This implies that 3D RT models, as opposed to

82   their ubiquitous 1D counterparts, will be required to make EarthCARE's radiative closure assess-

83   ment fruitful (Illingworth et al. 2015). Hence the need for 3D arrays of data that describe the Earth-

84   atmosphere system adjacent to the ~1 km-wide retrieved L2-cross-section.

85   Fortunately, BBR data are not bound to 10 km resolution, as point-spread function widths of its

86   native radiances are ~0.7 km. This offers much flexibility to the design of the closure assessment

87   (e.g., Tornow et al. 2018). The extreme case is to use a single along-track line of BBR radiances

88   that overlap, at best approximately, the ~1 km wide curtain of L2-retrieved profiles, referred to

89   hereinafter as the L2-plane. This would, however, degrade BBR performance, via reduced signal-

90   to-noise ratio and pointing accuracy, and thus weaken closure assessments. Alternatively, one

91   could attempt an across-track "broadening" of the L2-plane so as to cover as many BBR native

92   radiances as deemed necessary. Regardless of the route taken and the size of domains over which

93   closure assessments are to be performed, there is the ever-present related issue of lateral flow of

94   photons both within assessment domains *and* between assessment domains and their adjacent areas.

95   Taking these issues together, EarthCARE's science team opted for its closure assessment experi-

96   ment to use 3D RT models applied to assessment domains centred on the L2-plane with across-

97   track widths appreciably greater than 1 km (Illingworth et al. 2015).

98   The method for approximating 3D geophysical variables adjacent to the L2-plane, in order to

99   safely use both 3D RT models and BBR data, is the radiance-matching *Scene Construction Algo-*

100   *rithm* (SCA) (Barker et al. 2011), which forms the basis of the ACM-3D processor. The purpose

101   of the current paper is to recap, in section 2, the SCA, present several operational details associated

102   with it, and demonstrate, in section 3, its overall performance using simulated observations for a

103   virtual Earth-observation system (Qu et al. 2023; Donovan et al. 2023). Application of RT models

104   to SCA products and subsequent radiative closure assessments for the same virtual environments

105   are discussed by Cole et al. (2023) and Barker et al. (2023). A brief discussion is given in section

106   4.

107 2. 3D Atmosphere-Surface Scene Construction Algorithm

108   To begin, EarthCARE's products are partitioned into ~6,565 km long "frames", which makes six

109   frames / orbit. Position in a frame is defined by the Joint Standard Grid (JSG). Each frame contains

110   N_{JSG} L2-retrieved columns along-track. Frame widths are 150 km as defined by the MSI's swath;

111   35 km to the right and 115 km to the left of the L2-plane (relative to the satellite's direction of

112   motion). Some algorithms require data beyond nadir, and so each frame's files also contain n_ε

113   swaths of data from neighbouring frames. JSG coördinates are denoted as (i, j), with i running

114   along-track from $1 - n_\varepsilon$ to $N_{JSG} + n_\varepsilon$, and j running perpendicular to the L2-plane, which is located

115   at $j = 0$.

116   As documented by Cole et al. (2023), EarthCARE's radiative products are produced by 1D and

117   3D broadband RT models. Some of these products are used to perform radiative closure assess-

118   ments of L2-retrievals (see Barker et al. 2023). While 1D RT models are applied, in ACM-RT (see

119   Cole et al. 2023), to all non-corrupt columns in the L2-plane, their results are averaged over small

120   domains D, in processor ACMB-DF where radiative closure is assessed, referred to hereinafter as

121   *assessment domains*, whose along-track centres, at $j = 0$, are the L2-plane. Conversely, 3D RT

122   models operate directly on D and domain-average results are computed in ACM-RT and used in

123   ACMB-DF. The structure of D for $j \neq 0$ is defined by the 3D *Scene Construction Algorithm*

124   (SCA), which is explained in the following subsections. Along-track lengths of D, in terms of JSG

125   cells, are n_{assess} columns(pixels), while their across-track half-widths are m_{assess}, making full across-

126   track widths $2m_{assess} + 1$ columns(pixels). The initial plan is to fix m_{assess} and n_{assess} at 2 and 21,

127   respectively. Thus, D are $\sim 5 \times 21$ km, so their areal extents, regardless of location, are ~ 100 km^2,

128   which is what the BBR was designed to operate at (see Illingworth et al. 2015).

129   The operational SCA is made up of several sub-algorithms. At its core is definition of D at

130    $(i, j \neq 0)$ via MSI radiance-matching (Barker et al. 2011). Other crucial components include: def-

131   inition of buffer-zones around D, as required by the 3D RT models; screening and ranking of D

132   in an attempt to maximize the usefulness of the radiative closure assessment process; and estima-

133   tion of errors for TOA fluxes and radiances that stem from the radiance-matching algorithm. To

134   improve readability of the main text, many details of these sub-algorithms are presented in Appen-

135   dices. General results are shown and discussed in Section 3.

136
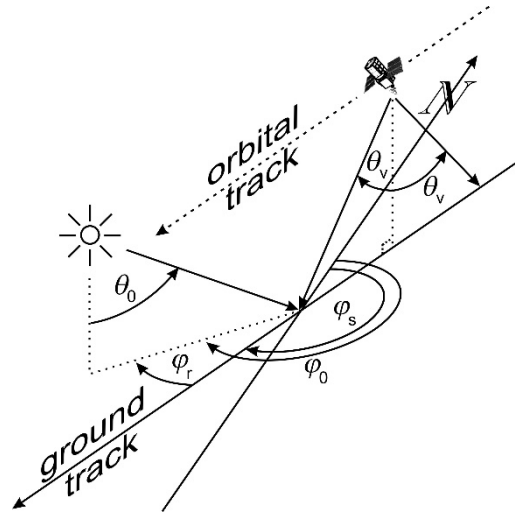
Figure 1: Schematic showing solar zenith angle θ_0, solar azimuth angle relative to north φ_0, sat-
ellite-tracking vectors relative to north φ_s, solar azimuth angle relative to satellite-tracking direc-
tion φ_r, and the BBR's two off-nadir zenith angles θ_v.

2.1. Radiance matching

The core of the SCA, and thus the ACM-3D processor, is passive narrowband radiance-matching
of an off-nadir MSI pixel's spectral radiances with their nadir counterparts along the L2-plane
(Barker et al. 2011). As this methodology has been described and used elsewhere (Barker et al.
2011; 2012; 2014; Sun et al. 2016), it is recapped briefly here, with details reiterated in Appendix
A. Note that all independent variables referred to here are available to the ACM-3D processor from
other EarthCARE processors; all of which are reported on in this special issue.

Let $r_k(i, j)$ be MSI radiances, for the kth channel, where values at position $(i, j = 0)$ align along the
L2-plane and have geophysical profiles associated with them. When seeking to populate an off-nadir
recipient column at $(i, j \neq 0)$ with a suitable *donor* from the L2-plane, the algorithm quantifies
how well $r_k(i, j \neq 0)$ match $r_k(m, j = 0)$ for all $m \in [i - M, i + M]$; M being the number of JSG

152 pixels, forward and backward, along the L2-plane one is prepared to allow the algorithm to search.

153 While M could depend on a host of variables, a default value of 200 has been used thus far. As

154 explained in Appendix A, for a nadir pixel to be a potential donor, the recipient's and donor's

155 surface types (land, sea, and snow/ice) must match, and cosine of solar zenith angles μ_0 and azi-

156 muth angles between Sun and satellite tracking direction φ_r must differ by less than specified

157 amounts. Figure *1* shows a schematic of solar-satellite geometry. While the recipient and L2-donor

158 pixels could be required to have the same cloud phase, the intention all along has been for the

159 algorithm to rely just on radiances, not other algorithms.

160   Of those L2-plane pixels whose MSI radiances best resemble those at $(i, j \neq 0)$, the one lying

161 physically closest to $(i, j \neq 0)$ becomes the donor, and its profiles of geophysical information get

162 replicated at $(i, j \neq 0)$. This procedure is performed for all $(i, j \neq 0)$ across the MSI's swath; pixels

163 at $(i, 0)$ donate to themselves. The result is *construction* of a 3D atmosphere-surface domain made-

164 up of profiles from the L2-plane. Correspondingly, MSI imagery are *reconstructed*, too. Figure *2*

165 shows a schematic of the radiance-matching procedure. Hereinafter, values at (i, j) that are based

166 on the SCA are indexed as $(m*(i, j), 0)$, which ties them back to the $m*(i, j)^{\text{th}}$ column/pixel along

167 the L2-plane.

168
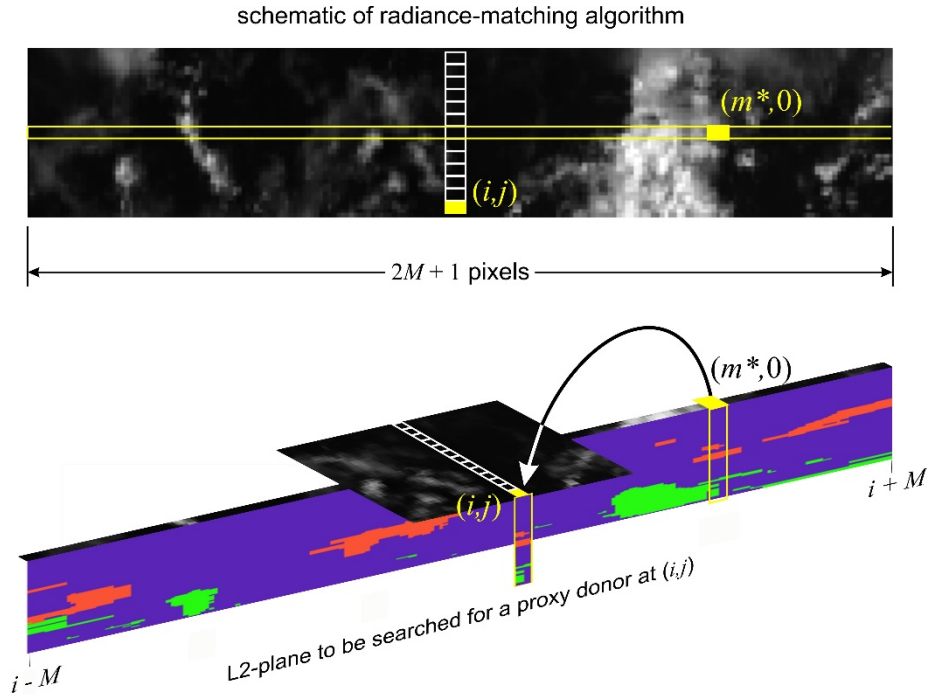
Figure 2: Top panel shows a swath of passive imagery and the location of an off-nadir pixel at (i,j) whose radiances match best with those along nadir at $(m^*,0)$. Lower panel is a schematic illustrating attribution of the (recipient) column associated with the pixel at (i,j) to the (donor) column of information inferred from EarthCARE's active-passive measurements at $(m^*,0)$.

2.2. Assessment domains and their buffer-zones

The 3D RT models used for EarthCARE employ cyclic horizontal boundary conditions. Real cloudy domains and those produced by the SCA are, however, non-cyclical and so when 3D RT models operate on them, adverse effects near the perimeter of D are affected by photon paths crossing discontinuous optical properties. One way to deal with this is to add atmosphere and surface to all edges of D so as to, not eliminate but rather, displace away from D any adverse effects set-up by the assumed cyclic boundary conditions. Hereinafter, the domain resulting from the combination of D and its buffer-zones is denoted as D^+.
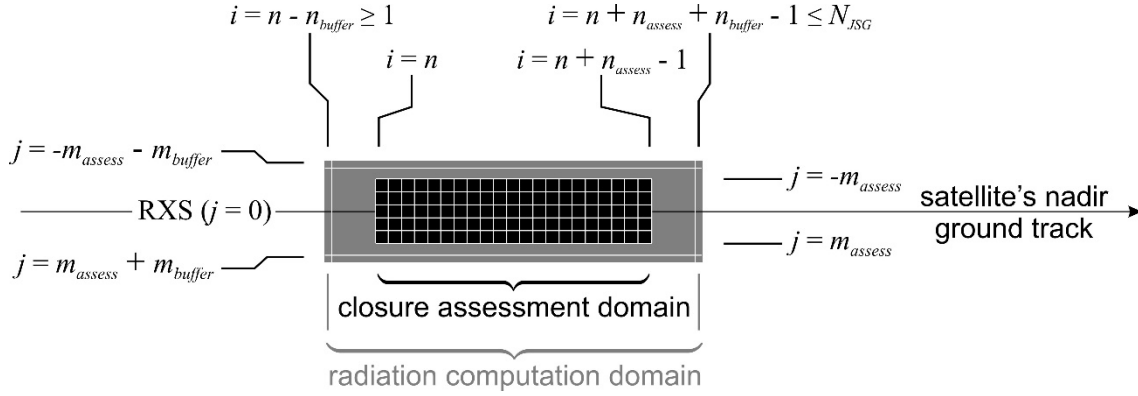
Figure 3: Schematic showing the radiative closure assessment domain $D(i)$ (black) and the radiation computation domain $D^+(i)$; the union of $D(i)$ and the buffer-zone (shaded). See the text for definitions of indices.

Buffer-zones also accommodate the fact that the BBR's oblique radiances associated with D consist partly of photons that were scattered by the atmosphere and surface outside of D. Barker et al. (2015) described an adjustment to 3D RT Monte Carlo models that approximates fractional contributions to a BBR radiance from photons whose last scattering event, by any particular scattering species, took place in D. Their algorithm, however, is too time-consuming for EarthCARE's official data processing system. Nevertheless, the buffer-zone should adequately capture contributions to BBR radiances that come from beyond D.

Setting the along- and across-track dimensions of buffer-zones is described in detail in Appendix B. *Figure 3* shows D, its associated D^+, and the indices that locate them on the JSG. The number of pixels in the along-track that are out in front $n_{buffer}^{\searrow}$ and trailing $n_{buffer}^{\swarrow}$ D can vary and depend on the minimum along-track buffer length $d_{\parallel}^{\min}$, assumed to be ~5 km, BBR viewing zenith angle θ_v, and nearby cloudtop altitudes $h(m*(i,j),0)$ as defined by the radiance-matching algorithm. Figure *4* is a schematic of this process which is detailed in Appendix B.
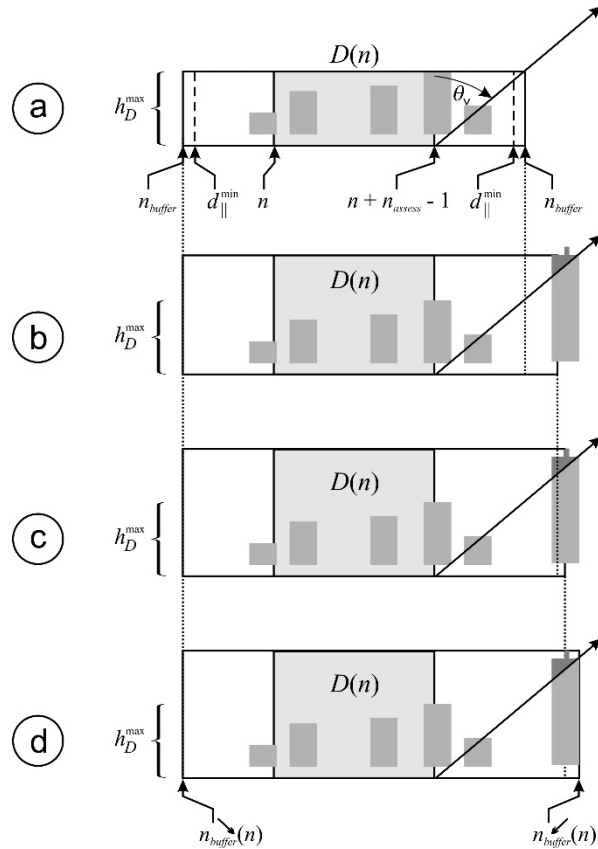
Figure 4: Schematic showing the procedure for finding along-track buffer-zone size; in this case $n_{buffer}^{\swarrow}$. (a) h_D^{max} is maximum cloudtop altitude in assessment domain D, and $d_{\parallel}^{min}$ is the smallest size buffer-zone allowed. (b) As the algorithm searches out in front of D, a cloud is encountered; part of which lies between D and the satellite, and so the buffer-zone increases. (c) Continuing the search, still a higher cloud is encountered between D and the satellite, thus increasing the buffer-zone further. (d) There is still more cloud between D and the satellite so the buffer-zone increases again, this time to its final value of $n_{buffer}^{\swarrow}$, despite the possibility of cloudtops further out being higher yet still. See text and Appendix B for details.

Note that $n_{buffer}^{\swarrow}$ and $n_{buffer}^{\searrow}$ are independent of θ_0. This is because for EarthCARE's orbit, over

80% of observations with $\theta_0 < 90°$ have $30° < \varphi_r < 150°$ implying that, for most cases, projection

of direct-beam (and hence cloud shadows) into the along-track walls of D will be small. Excep-

tions are for very large θ_0 with $\varphi_r < 30°$ or $\varphi_r > 150°$, but these cases are usually avoided because

the RT models rely on the plane-parallel approximation.
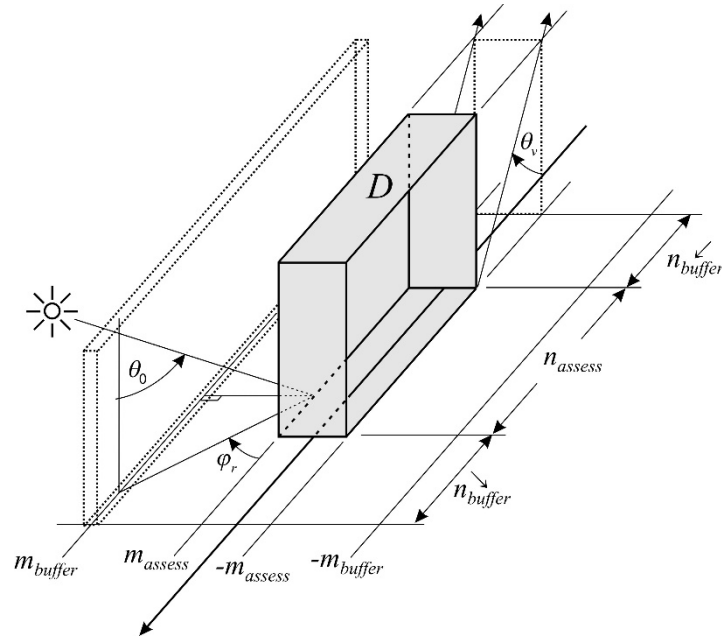
Figure 5: Schematic showing the procedure for finding the size of the cross-track buffer-zone size m_{buffer} . See text and Appendix B for details.

Determination of the size of cross-track buffer-zones m_{buffer} depends on $h\left(m*(i,j),0\right)$ adjacent

to the sunlit side of D and minimum size for the across-track buffer-zone $d_{\perp}^{\min}$. If a cloud to the

side of D casts a shadow that falls onto the region formed by D and its along-track buffer-zones,

then the cross-track buffer-zone extends to include the cloud doing the shadowing. Unlike the

along-track, m_{buffer} gets applied to both sides of D. Figure 5 summarizes definition of m_{buffer}.

2.3. Screening radiative closure assessment domains

Due to computational limitations and time constraints on product production, it is anticipated that

only a small number of D per frame will participate in the 3D RT radiative closure exercise (i.e.,

processor ACMB-DF). Hence, D that emerge from the SCA must be "screened and ranked" to

ensure that an adequate range of cases, from "simple" to "complex", be assessed in order to: i)

231 provide well-rounded pictures of algorithmic performances; ii) gauge whether mission objectives

232 are being met; and iii) provide guidance to data users who wish to focus on select conditions. At

233 the same time, screening and ranking should be flexible enough to be changed during the mission.

234 For instance, "simple" scenarios are likely to be of particular interest during the commissioning

235 phase (e.g., mono-phase, single-layer, overcast clouds).

236 The screening process eliminates D that are likely to yield uninformative assessments. It has

237 three stages as described in the following subsections. Each frame has two sets of surviving assess-

238 ment domains: D_{1D} contains domains that 1D RT results are averaged over; D_{3D} contains domains

239 that 3D RT models get applied to. Domains in D_{1D} and D_{3D} consist, respectively, of *radiative*

240 *assessment domains* D and *radiative computation domains* D^+ (see Figure *3*).

241 *2.3.1. Screening Stage 1: Failed retrievals and corrupt data*

242 If there are corrupt data or failed retrievals for any column in either D or D^+, the domain will not

243 be forwarded to subsequent processes. This is because they simply cannot be used by 3D RT mod-

244 els. Examples of failed retrievals include algorithms that did not converge to a solution or con-

245 verged to values that are out of bounds. Corrupt data, on the other hand, includes failure at the L1

246 level and data corrupted during transmission.

247 *2.3.2. Screening Stage 2: Geophysical conditions*

248 *a) Solar zenith angle*

249 Generally speaking, solar RT becomes increasingly complicated as solar zenith angle θ_0 increases.

250 This is because: i) radiances and fluxes for EarthCARE-sized domains will depend increasingly on

251   conditions outside D and D^+; and ii) Earth's sphericity becomes increasingly important; Earth-

252   CARE's RT codes are plane-parallel models. Not only do large θ_0 impact the SCA directly, they

253   stress retrieval algorithms that use MSI data. Hence, when the Sun is up, D or D^+ must have

254
$$\max\{\theta_0(i,j)\} < \theta_0^* \quad \forall (i,j) \in D \text{ or } D^+, \tag{1}$$

255   where θ_0^* is the maximum allowed value of θ_0, in order for solar radiances to be considered by the

256   SCA. Initially, $\theta_0^* = 75°$. When the Sun is down, however, data from solar channels are simply not

257   used; as shown by Barker et al. (2011), this diminishes the SCA's performance.

b) Single surface type

259   To focus closure assessments on retrieved cloud and aerosol properties, and reduce potential com-

260   plications due to boundary conditions that are outside the purview of EarthCARE's retrievals, D

261   and D^+ must have at least 90% of its area occupied by a single broad class of surface type. These

262   types are: water (oceans and lakes), land, and ice.

c) Homogeneous land surfaces

264   Each JSG pixel has a land-type designation obtained from the International Geosphere–Biosphere

265   Programme (USGS 2018). Let f_ℓ be the fraction of JSG pixels in either D or D^+ that corresponds

266   to the ℓth surface-type. For reasons listed above, if D and D^+ is a "land" domain, then for them to

267   be included in $\mathsf{D}_{1\mathrm{D}}$ and $\mathsf{D}_{3\mathrm{D}}$, they must have

268
$$\max\{f_\ell\} > f^*, \tag{2}$$

269   where f^* is set initially to 0.9.

270   *d) Surface elevation*

271   Uncertainties in spectral bidirectional reflectance and emittance functions as well as albedos and

272   emissivities are complicated by variations in surface elevation. In an attempt to limit uncertainties

273   associated with the setting of these lower boundary conditions in the RT models, only very flat

274   assessment domains are allowed. Hence, if σ_{srf} is standard deviation of surface elevation for D or

275   D^+, then for them to be included in $\mathbf{D}_{1D}$ and $\mathbf{D}_{3D}$, they must have

276
$$\sigma_{srf} < \sigma_{sfc}^*, \tag{3}$$

277   where σ_{sfc}^* is set initially to 0.1 km.

278   *2.3.3. Screening Stage 3: Quality of radiance matching*

279   Where SCA reconstructed MSI radiances are poor, it is reasonable to assume that corresponding

280   constructed 3D domains are, too. Thus, the final screening stage addresses the quality of recon-

281   structed MSI imagery, but it also provides bias-correction estimates for modelled TOA quantities.

282   For an assessment domain D of n_{assess} JSG pixels along-track and $j \in \left[-m_{assess}, m_{assess}\right]$ across-

283   track, the nth moment of r_k over D, excluding the L2-line along $j = 0$, is

284
$$\left\langle r_k^n \right\rangle = \frac{1}{2m_{assess}n_{assess}} \sum_{i=i_1}^{i_1+n_{assess}-1} \sum_{j\in[-m_{assess},-1]\cup[1,m_{assess}]} r_k^n(i,j). \tag{4}$$

285   where i_1 is along-track JSG index at the edge of D. Corresponding reconstructed values are

286
$$\left\langle \hat{r}_k^n \right\rangle = \frac{1}{2m_{assess}n_{assess}} \sum_{i=i_1}^{i_1+n_{assess}-1} \sum_{j\in[-m_{assess},-1]\cup[1,m_{assess}]} r_k^n(m*(i,j),0). \tag{5}$$

287   Therefore, errors stemming from the radiance-matching algorithm, for the kth MSI channel, are

288
$$\Delta\left\langle\hat{r}_k^n\right\rangle = \left\langle\hat{r}_k^n\right\rangle - \left\langle r_k^n\right\rangle. \tag{6}$$

289   Let $\left\langle F_{\text{SW}}\right\rangle$ and $\left\langle F_{\text{LW}}\right\rangle$ be TOA shortwave (SW) and longwave (LW) fluxes, averaged over D,

290   as estimated by angular direction models in the BMA-FLX processor (Velázquez-Blázquez et al.

291   2023). Since MSI radiances r_1 (0.67 μm) and r_6 (10.80 μm) often correlate well with $\left\langle F_{\text{SW}}\right\rangle$

292   and $\left\langle F_{\text{LW}}\right\rangle$ (Barker et al. 2014), TOA flux bias errors due to the radiance-matching algorithm can

293   be approximated as

294
$$\Delta\left\langle\hat{F}_{\text{SW}}\right\rangle \approx \left\langle F_{\text{SW}}\right\rangle\frac{\left\langle r_1\right\rangle - \left\langle\hat{r}_1\right\rangle}{\left\langle\hat{r}_1\right\rangle} \quad\text{and}\quad \Delta\left\langle\hat{F}_{\text{LW}}\right\rangle \approx \left\langle F_{\text{LW}}\right\rangle\frac{\left\langle r_6\right\rangle - \left\langle\hat{r}_6\right\rangle}{\left\langle\hat{r}_6\right\rangle}. \tag{7}$$

295   If these values satisfy

296
$$\left|\Delta\left\langle\hat{F}_{\text{SW}}\right\rangle\right| > \Delta F_{\text{SW}}^* \mu_0 \quad\text{and}\quad \left|\Delta\left\langle\hat{F}_{\text{LW}}\right\rangle\right| > \Delta F_{\text{LW}}^*, \tag{8}$$

297   where ΔF_{SW}^* and ΔF_{LW}^* are tolerable broadband TOA flux errors arising from the radiance-match-

298   ing algorithm, D is *not* included in neither D_{1D} nor D_{3D}. Both $\Delta\left\langle\hat{F}_{\text{SW}}\right\rangle$ and $\Delta\left\langle\hat{F}_{\text{LW}}\right\rangle$ get passed to

299   ACMB-DF and used to bias-correct estimated TOA fluxes made by both 1D and 3D RT models.

300   This completes the screening processes leaving D_{1D} and D_{3D} with m_{1D} and m_{3D} assessment do-

301   mains, respectively.

302   *Table 1* provides a glimpse into success rates of D and D^+, in all three frames, for the screenings

303   just described using conditions as summarized in the table. Of course, overall success rate for

304    $\theta_0 < 75°$ will be much smaller than most reported here owing to these being "descending" frames.

305 Note also the tendency for success rates for D^+ to be less than those for D. This is because the areal

306 extents of D^+ are always larger than that for D.

307 **Table 1.** Success rates of D and D^+ for the three frames that meet the conditions as listed.

		Halifax		Baja		Hawaii	
screening variable	**condition**	D	D^+	D	D^+	D	D^+
cloud retrieval quality	more than 10% of columns have valid retrievals	97	98	96	97	97	99
flux reconstruction	both $\Delta F_{SW}^* \mu_0$ and $\Delta F_{LW}^* =$ 5 W m^{-2} (see (8))	100	94	100	93	100	82
solar zenith angle	$\theta_0 < 75°$ or $\theta_0 > 90°$	63	59	100	100	100	100
land-sea/water	single type of land/water for at least 90% of a domain	90	90	84	80	100	100
surface type*	surface type for at least 90% of a domain; sunglint occurs for at most 20% of a domain	94	92	84	81	52	49
land surface elevation	standard deviation < 100 m	95	97	79	70	100	100

308

2.4. Ranking radiative assessment domains

310 As noted above, the EarthCARE mission will provide near-real time products with limited compu-

311 tational resources. The portion of the processing chain constrained most by this involves 3D SW

312 RT models. For them to achieve adequate signal-to-noise ratios, just a small fraction of the thou-

313 sands of potential D^+ per frame can be assessed. Thus, to enhance efficacy of the radiative assess-

314 ment process, an algorithm was developed that ranks D^+ in D_{3D}. At any time, ranking can be

315 overruled manually, such as when testing during commissioning phase. The ranking algorithm that

316 was decided upon samples cloud scenarios in proportion to relative frequencies of occurrence.

317   For the initial version of the algorithm, 1 km resolution MODIS-retrieved values (MYD06_L2)

318   of cloud optical depth τ_{cld} and cloudtop pressure p_{cld}, inferred from measurements made during

319   2020, were grouped into 5 x 21 km arrays, to match EarthCARE's planned 5 x 21 km domains D,

320   and for each array, mean values $\langle \tau_{cld} \rangle$ and $\langle p_{cld} \rangle$ were computed along with total cloud fraction

321   A_c (Platnick et al. 2015). They were then assigned to bins defined by $10°$ ranges of latitude and

322   longitude, and ranges for $\langle \tau_{cld} \rangle$, $\langle p_{cld} \rangle$, A_c, and time of observation of

323

$$
\begin{aligned}
\langle \tau_{cld} \rangle \quad &: \quad (0,4];(4,23];(23,150] \\
\langle p_{cld} \rangle \quad &: \quad (0,440];(440,680];(680,\infty) \\
A_c \quad &: \quad (0,0.25];(0.25,0.75];(0.75,0.99];(0.99,1] \\
time \quad &: \quad DJF;MAM;JJA;SON
\end{aligned}
\tag{9}
$$

324   Since only cloud-bearing domains need be ranked, the number of applicable bins is 23,328, of

325   which the nth has N_n domains. When $\theta_0 \geq 90°$, $\langle \tau_{cld} \rangle$ is not retrieved, so the same ranking proce-

326   dure uses the remaining three variables only. Radiative closure assessments for SW fluxes are not

327   done when $75° < \theta_0 < 90°$ on account of too many overwhelming uncertainties with retrievals and

328   plane-parallel RT modelling. Thus, domains in this range are not ranked.

329   For EarthCARE frames with 6,400 1-km L2 columns in the L2-plane there is the potential for

330   6,400 - 21 + 1 = 6,380 (over-sampled) assessment domains, each of which falls into one of the

331   MODIS bins. Now, using only domains with $A_c > 0.01$, form the frame-specific cumulative fre-

332   quency such that the ith domain has a value

333

$$
\mathsf{N}(i) = \frac{1}{\mathsf{N}(6,380)} \sum_{j=1}^{i} N_n(j) \quad ; \quad i = 1,\ldots, N_{cld} \leq 6,380.
\tag{10}
$$

334   Then, generate a uniform pseudo-random number $R \in (0,1]$ and find the closest $N(i)$; this iden-

335   tifies the top-ranked D^+. This is repeated, without replacement, until (possibly all) the domains are

336   ranked. The resulting lists are passed on to ACM-RT.

3. Results

338   The SCA's sub-algorithms are discussed in series in this section. The only part not evaluated here

339   is the ranking algorithm (see section 2.4). Its performance is demonstrated in Cole et al. (2023; in

340   this issue) where radiative transfer models act on the highest ranked assessment domains.

3.1. Reconstruction of passive radiances

342   Radiance matching is the essence of the SCA, and a sampling of results is provided here. More

343   details are in Barker et al. (2011; 2012; 2014) and Sun et al. (2016). All results presented here, and

344   when $\theta_0 < 90°$, come from using MSI channels: 1 (0.67 μm), 4 (2.21 μm), 5 (8.80 μm), and 7

345   (12.00 μm); i.e., $K_s = 4$ in (11). Obviously, when $\theta_0 \geq 75°$ the SW channels are not used. The

346   largest impediment facing this algorithm is when conditions off the ground-track (GT) differ much

347   from the relatively few samples along the GT (Barker et al. 2011). Figure *6* shows a full-width

348   segment of the *Hawaii* frame that contains both catastrophic failure due to inadequate conditions

349   along the GT and excellent performance for the opposite reason. Approximately 50 - 100 km east

350   of the GT, between 9.5°N and 13°N, radiances, especially channel 1's, that are associated with

351   much cloud are severely short-changed on account of a long stretch of near-cloudless conditions at

352   nadir. To partially remedy this, the algorithm would have to be permitted to search the GT much

353   further than 200 km, as in this example, but in so doing it would run the risk of identifying donor

354 columns associated with increasingly different meteorological conditions. On the other hand, be-

355 tween 5°N and 8°N performance is extremely good across the entire 150 km wide frame.
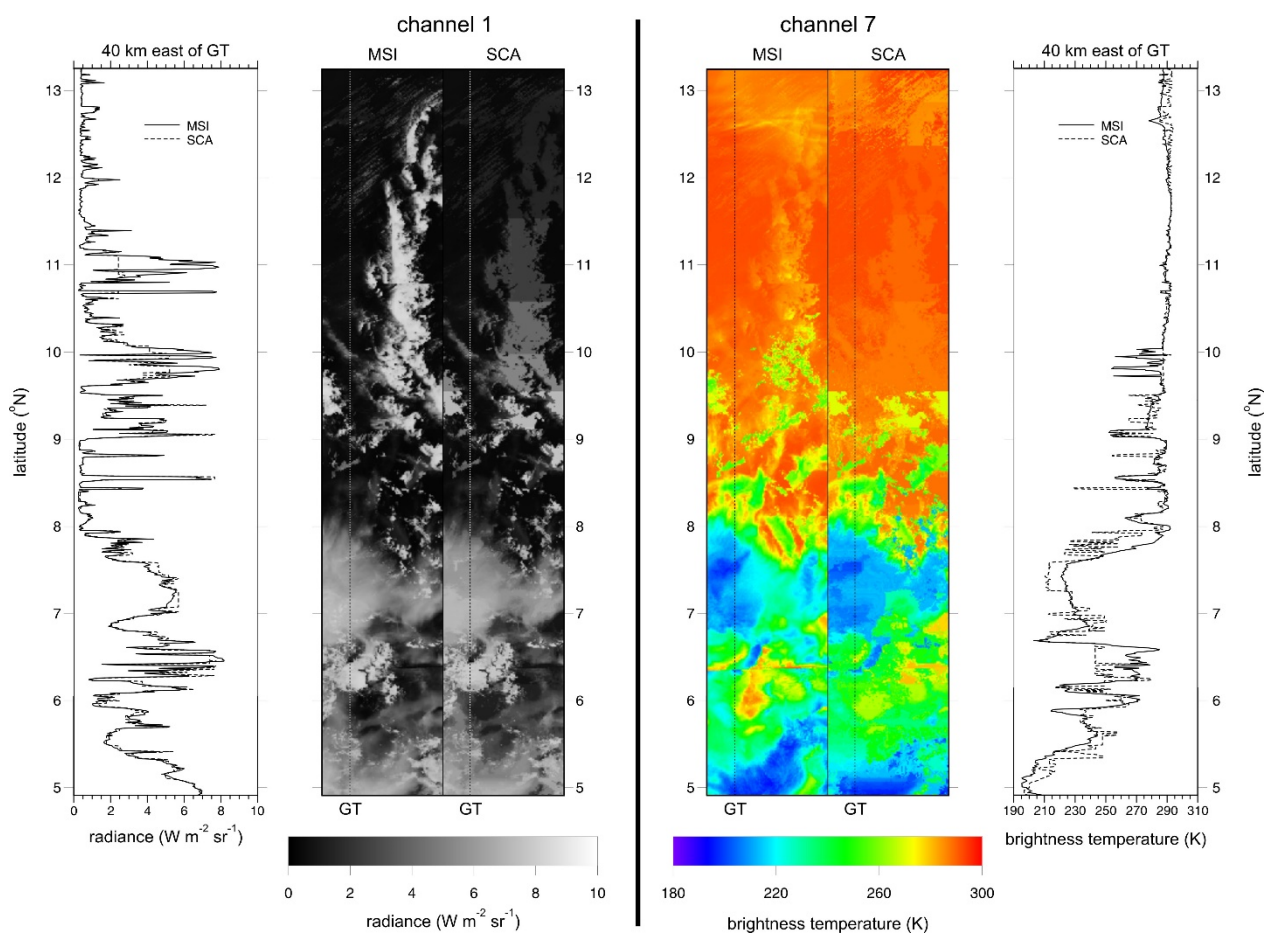
356

357 **Figure 6:** Left panel shows MSI and corresponding SCA channel 1 radiances for a segment of
358 the *Hawaii* frame measuring 150 km wide and 900 km long. Right panel is corresponding bright-
359 ness temperatures from channel 7 radiances. Dashed lines marked GT indicate the ground-track
360 at nadir, which coincides with the L2-plane. Line graphs show MSI and SCA values along the
361 centres of the domains, which are 40 km east of GT.

362
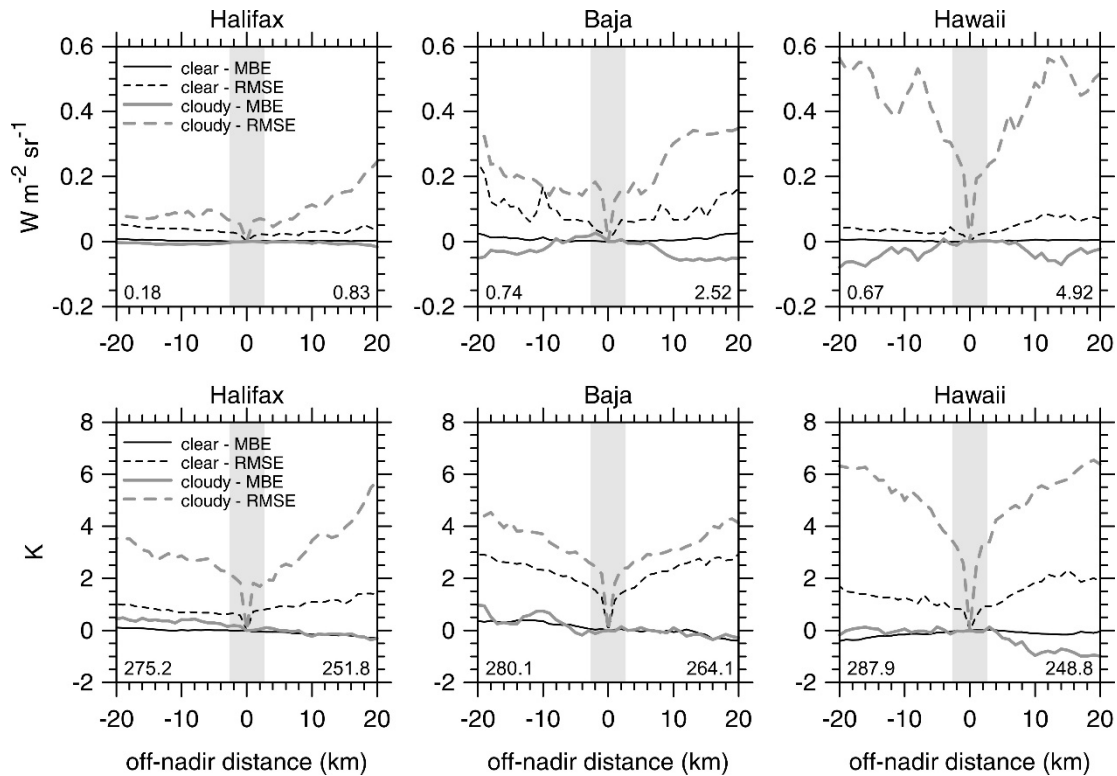
Figure 7: Full-frame mean bias errors (MBE) and root mean square errors (RMSE) for SCA re-constructed radiances as functions of distance (-ve values are W) from the ground-track (GT in *Figure 6*). Upper and lower rows are for MSI channel 1 radiances and 7 brightness temperatures. Full-frame mean values are listed on the base of each plot: clear-sky on the left, cloudy-sky on the right. Grey bands indicate EarthCARE's default assessment domains.

Figure *7* shows mean bias errors (MBE) and root mean square errors (RMSE) for reconstructed MSI channels 1 and 7 as functions of distance, east and west, of GT for the full lengths of the three test frames (see Qu et al. 2023). By definition, MBE and RMSE along GT are zero. For channel 1's reconstructions, MBEs out to ±20 km are generally smaller than 0.05 W m⁻² sr⁻¹, with smaller errors for cloudless pixels. The negative biases for *Baja* and *Hawaii* frames out past ~ 5 km from GT stem from clouds along the GT being slightly darker than those elsewhere over the frames (see Figure *6*). Likewise, MBEs for channel 7 are generally smaller than 0.5 K. Over the 5 km wide assessment domains centred on GT, MBEs for both channels are almost negligible relative to the frame-wide average values that are listed along the base of each plot.
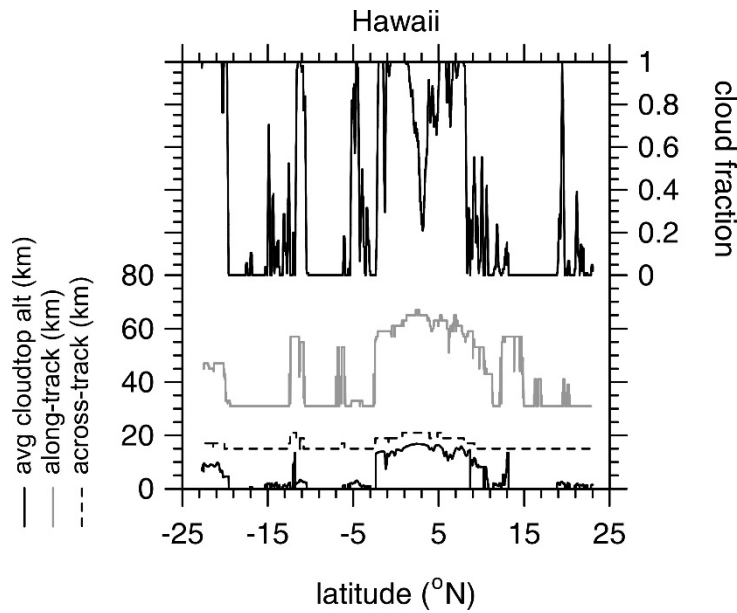
Figure 8: Along-track and across-track length of assessment domain plus buffer-zones as functions of latitude for the *Hawaii* frame. All assessment domains are 5 km across-track by 21 km along-track. Minimum size for all buffer-zones is 5 km. Also shown are corresponding values of mean cloudtop altitude and cloud fraction for 5 x 21 km assessment domains.

Unlike MBEs, however, RMSE values jump immediately off the GT. In general, they continue

to increase with distance from GT, but it is difficult to say at what distance they become unusable.

It is important to note that RMSE values plotted here get reduced by at least a factor of 10 for

averages over assessment domains.

3.2. Definition of assessment domain buffer-zones

The planned initial default values for both $d_{\parallel}^{\min}$ and $d_{\perp}^{\min}$ is 5 km. Thus, for D measuring 5 x 21

km, 3D RT will be applied to D^+ that measure at least ~15 km across-track by ~31 km along-track.

Figure *8* shows sizes of D^+ along the *Hawaii* frame. The most notable feature is that along-track

lengths vary much more than across-track lengths. This is driven by the fixed along-track off-nadir

views of the BBR; whenever cloud occurs, especially high cloud, values of $n_{buffer}^{\searrow}$ and $n_{buffer}^{\swarrow}$ exceed

395 0. Lengths of D^+ maximize between about $3°$N and $6°$N where mean cloudtop altitudes h reach

396 ~17 km; this despite cloud fractions for D^+ being substantially less than 1.

397  While across-track buffer sizes m_{buffer} depend on h, too, they also depend on φ_r and θ_0. Near

398 latitude $10°$N, while $\varphi_r \approx 107°$(Sun is shining in almost perpendicular to GT), $\theta_0 \approx 30°$ and so

399 lengths of cloud shadows cast perpendicular to GT are small. As such, there is little need to expand

400 the domain across-track, and so $m_{buffer} = 0$ and cross-track size of D^+ equal the default 15 km.

401 Near latitude $21°$S, however, where mean h are the same as near $10°$N, clouds are more overcast,

402 but equally important, $\varphi_r \approx 130°$, which is still not far off shining in perpendicular to GT, and

403 $\theta_0 \approx 50°$. Together these conspire to cast cloud shadows well beyond D resulting in D^+ that are

404 slightly larger than the default.

405 **3.3. Estimation of SCA-related bias errors for TOA broadband fluxes**

406 In a manner similar to cloud radiative effects, estimation of errors for TOA broadband radiative

407 fluxes that arise from the SCA process provide a simple, integrated indication of SCA performance.

408 Figure *9* shows cumulative frequency distributions of $\Delta\langle \hat{F}_{SW} \rangle$ and $\Delta\langle \hat{F}_{LW} \rangle$ (see (7)), for the *Ha-*

409 *waii* frame. Errors for this frame are the largest of the three. As is often the case, errors tend to be

410 largest for SW fluxes, and increase slightly as assessment domain A_c increases. The latter point

411 basically indicates that the SCA does extremely well in clear-sky conditions; even for the *Baja*

412 frame that was mostly over variable land.

413
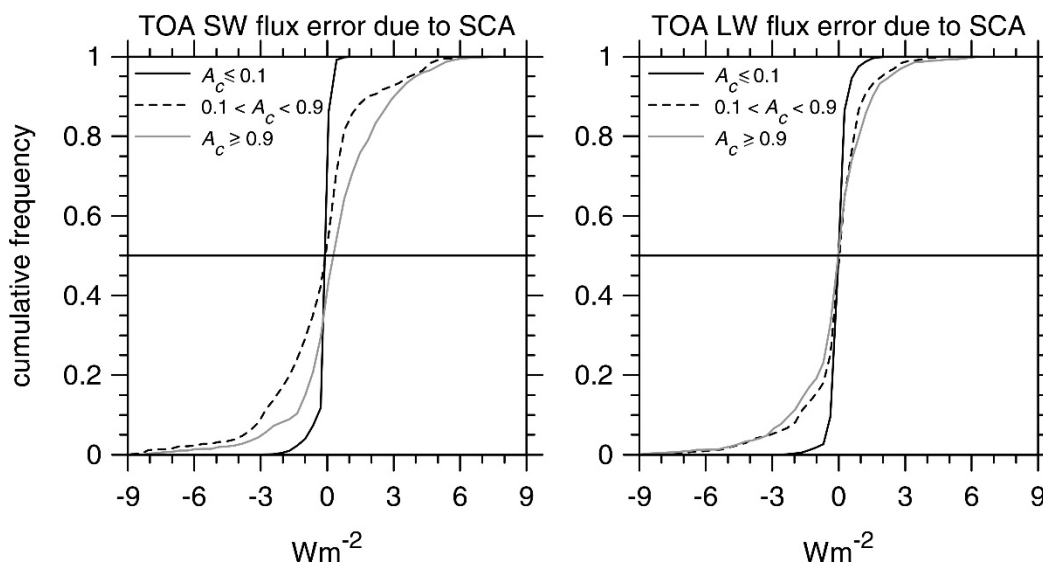
Figure 9: Cumulative frequency distributions of estimated errors in broadband TOA upwelling
SW and LW fluxes stemming from the SCA for all 5 x 21 km assessment domains in the *Hawaii*
frame. Distributions are partitioned for three ranges of assessment domain total cloud fraction A_c.

417

It is encouraging to see that median errors for both bands are negligible for all conditions. More-
over, as Figure *9* shows, with ~90% of errors being within ± 3 W m^{-2}, and slightly better for the
other frames, errors imparted on TOA flux estimates by the SCA will not hinder assessment of
EarthCARE's objective of retrieving cloud-aerosol properties well enough as to be able to model,
on average, TOA fluxes to within ± 10 W m^{-2}.

4. Summary and discussion

The EarthCARE satellite mission has set itself a very high bar with its plan to infer cloud and
aerosol properties, from its observations, well enough that when used to initialize radiative transfer
(RT) models, their estimates of TOA fluxes will differ from observed values by, typically, less than
± 10 W m^{-2}. To realize, and gauge the success of, this *radiative closure assessment* it will be nec-
essary to employ, operationally, 3D atmospheric RT models. This by itself will set EarthCARE

429   apart from its predecessors, which have relied entirely on 1D RT models. The immediate issue

430   facing this plan is that L2-retrievals at nadir are just ~1 km wide, and at this scale net fluxes of

431   lateral flowing radiation, not accounted for by 1D RT models, can be substantial (e.g., Marshak et

432   al. 1998). To justifiably use 3D RT models, however, the atmosphere-surface system has to be

433   defined on both sides of the narrow L2-plane. The point of this paper was to demonstrate Earth-

434   CARE's method of expanding its L2-retrievals perpendicular to the L2-plane. At the core of this

435   *3D scene construction algorithm* (SCA) is a radiance-matching (RM) scheme that uses Earth-

436   CARE's MSI passive imagery (cf. Barker et al. 2011; 2012; 2014). There are, however, other as-

437   pects of this process that have been documented here for the first time.

438   Synthetic radiances measured virtually by EarthCARE's MSI for three test frames, which were

439   produced for *end-to-end simulation* of EarthCARE's measurement-processing chain (see Qu et al.

440   2023), were used here to demonstrate the performance of the SCA. "Reconstruction" of measured

441   MSI radiances forms the foundation of the SCA. Basically, off-nadir pixels are paired with a nadir

442   pixel whose spectral radiances best match theirs. The 3D domains to be used by the 3D RT models

443   are "constructed" by taking columns of geophysical information associated with matching nadir

444   pixels and inserting them at the off-nadir pixels.

445   Comparing reconstructed radiances to their observed counterparts provides a straightforward

446   indication of the success of the SCA. If observed radiances are reconstructed poorly, one has to

447   also assume that correspondingly constructed 3D surface-atmosphere domains are unfit for both

448   3D RT models and radiative closure assessment. SCA errors flare-up when conditions needed at

449   off-nadir locations are lacking from the nearby the L2-plane. Typical performances of the SCA

450   were shown in Section 3.1, and as expected, generally erode the further recipient pixels are from

451   their donors. This is not much of an issue for radiative assessment domains themselves, for they

452   extend just 2 km from the L2-plane. Their buffer-zones, however, which were described in section

453   2.2, can be as much as 10 km from the L2-plane (see Figure *3*). The reason why assessment do-

454   mains are so small is because EarthCARE's radiative closure assessment seeks to verify the narrow

455   L2 retrievals, not the SCA; the SCA should help achieve this as invisibly as possible.

456   Once defined, assessment domains and their buffer-zones get screened (see section 2.3) in an

457   attempt to identify those most likely to realize useful closure assessments. Furthermore, the inter-

458   section of EarthCARE's data processing limitations with the computational demand of the 3D solar

459   RT model (Cole et al. 2023) forces the need to rank assessment domains to ensure that the few that

460   get assessed per frame lead to good samplings, over the mission's life, of conditions that occur over

461   the globe and the year. This process was described in section 2.4.

462   The simple method of estimating TOA flux bias errors that are likely to arise from the SCA

463   (Barker et al. 2014) was assessed using test frame synthetic observations. Reassuringly, it was

464   shown in Section 3.3 that most TOA flux errors due to the SCA's imperfect atmospheres, for as-

465   sessment domains measuring 5 x 21 km, can be expected to be much smaller, and rarely larger,

466   than EarthCARE's stated goal of ± 10 W m^{-2}.

467   To conclude, it is tempting to view the SCA as a very cost-effective (i.e., almost free) *scanning*

468   *active sensor system* (cf. Illingworth et al. 2018). But one almost always gets what one pays for,

469   and the SCA is, when pushed, no exception. Its performance, especially well-removed from the

470   L2-plane, cannot be expected to rival that of an authentic scanning active sensor system (Barker et

471   al. 2021); to use it as a full-up replacement would be cavalier. In its current role, however, as

472   purveyor of approximate, ancillary information that both facilitates use of 3D RT models and

473   strengthens verification of L2 retrievals, it appears as though its shortcomings will be tolerable and

474   outweighed by its benefits.

475   **Acknowledgements**

476   Work reported on in this paper was funded by the European Space Agency and in-kind support

477   from ECCC. This paper, and studies leading to it, benefited much from numerous discussions with

478   Dr. Tobias Wehr who passed away on 1-Feb-2023.

479

480   **Data availability**

481   Data used in this report, and in other EarthCARE reports in this issue, can be obtained at van Za-

482   delhoff et al. (2022).

483

484   APPENDIX A

485   **Radiance-matching algorithm**

486   Let $r_k(i,j)$ be MSI radiance, for the kth MSI channel, at (i, j) on the joint standard grid (JSG) in which

487    $j = 0$ is along the L2-plane. Following Barker et al. (2011), when seeking to populate a column at

488    $(i, j \neq 0)$ with a suitable proxy from $(i, j = 0)$, begin by computing, for K_s channels,

$$F(i,j;m) = \Lambda(i,j;m) \sum_{k=1}^{K_s} a_k \left[\frac{r_k(i,j) - r_k(m,0)}{\max[r_k(i,j), r_k(m,0)]} \right]^2 \quad ; \quad m \in [i-M, i+M]; j \notin 0, \quad (11)$$

490   where $(m,0)$ holds potential *donor* profiles for the *recipient* at $(i, j \neq 0)$, a_k are weights that could

491   depend on channel but were assumed to equal 1, and M is number of pixels, forward and backward,

492   along the L2-plane to be searched for a donor. The function $\Lambda(i, j;m)$ is defined as

$$\Lambda(i,j;m) = \begin{cases} -1 & ; \quad \chi = .false. \\ 1 & ; \quad \chi = .true. \end{cases} \quad (12)$$

494   By requiring

$$\chi = \begin{cases} \text{surface at } (i,j) = \text{surface at } (m,0) \\ \qquad .and. \\ \left| \mu_0(i,j) - \mu_0(m,0) \right| < \Delta\mu_0 \\ \qquad .and. \\ \mu_0(i,j) \cdot \mu_0(m,0) > 0 \\ \qquad .and. \\ \left| \varphi_r(i,j) - \varphi_r(m,0) \right| < \Delta\varphi_r \\ \qquad .and. \\ m \in [1, N_{JSG}], \end{cases} \quad (13)$$

496   it controls whether or not a pixel at $(m,0)$ is to be considered as a potential donor (see section 2.3).

497   The upper condition means that surface types (land, sea, and snow/ice) must be the same at (i,j)

498   and $(m,0)$. The next two conditions mean that at (i,j) and $(m,0)$ cosine of solar zenith angles μ_0

499   must differ by less than $\Delta\mu_0 = 0.005$, and the Sun must be up or down at both locations. Next, the

500   difference between solar azimuth angles relative to the satellite's tracking direction φ_r must be less

501   than $\Delta\varphi_r = 5°$. The final condition simply means that the search cannot go past the ends of a frame.

502   It almost goes without saying, but when the Sun is down at $(m,0)$, SW radiances are simply not

503   used in (11).

504   For the $1 \le M' \le 2M+1$ values of $F(i,j;m) \ge 0$ that get computed, define Euclidean distances

505   between the centres of (i,j) and $(m,0)$ as

506
$$L(i,j;m) = \Delta L\left[(i-m)^2 + j^2 \right]^{1/2},$$
(14)

507   where ΔL is horizontal resolution, which for EarthCARE is ~1 km, and sort $F(i,j;m)$ from small-

508   est to largest (i.e., best to worst radiance match), with $L(i,j;m)$ going along passively. Denote the

509   reordered sequences as $\left\{\hat{F}(i,j;m)\right\}_{m=1}^{M'}$ and $\left\{\hat{L}(i,j;m)\right\}_{m=1}^{M'}$. Finally, the donor for location $(i,j \ne 0)$

510   is deemed to reside at

511
$$m^*(i,j) = \arg\min_{m\in[1,M'\cdot f]}\left\{\hat{L}(i,j;m)\right\}$$
(15)

512 which reads: find m that corresponds to the smallest distance between the recipient at (i, j) and those

513 pixels that constitute the smallest $100f\%$ of $\hat{F}(i, j; m)$. The tuneable parameter f will be set initially to

514 0.05, but this could change (see Barker et al 2011). The procedure outlined here is performed for all

515 $(i, j \neq 0)$ across the MSI's swath, with pixels at $(i, 0)$ donating to themselves.

516

517 APPENDIX B

518 **Calculation of buffer-zone sizes**

519 *a. Along-track length*

520 Let $h\big(i*(i,j),0\big)$ be cloudtop altitude at JSG cell (i,j) using the SCA's field. Using these values,

521 define for each i in a frame the highest cloudtop in across-track swaths of JSG pixels spanning the

522 assessment domains as

$$h_{\perp}^{\mathrm{max}}(i)=\max\big\{h\big(i*(i,j),0\big)\big\}:j\in\big[-m_{assess},m_{assess}\big]. \tag{16}$$

524 The symbols $\perp$ and $\parallel$ indicate across- and along-tracks, respectively. Thus, maximum cloudtop

525 altitude in an assessment domain $D(n)$ is

$$h_{D}^{\mathrm{max}}(n)=\max\big\{h_{\perp}^{\mathrm{max}}(i)\big\}:i\in\big[n,n+n_{assess}-1\big]. \tag{17}$$

527 Consider first the buffer-zone out in front of $D(n)$; applicable most to the BBR's backward

528 view. The minimum number of JSG pixels that one need be concerned about searching to see if

529 clouds outside of $D(n)$ obscure part of $D(n)$ is

$$n_{buffer}=nint\left(\frac{\max\big\{d_{\parallel}^{\mathrm{min}},h_{D}^{\mathrm{max}}(n)\tan\theta_{v}\big\}}{\langle\Delta x\rangle}\right), \tag{18}$$

531 where $d_{\parallel}^{\mathrm{min}}$ is the absolute minimum along-track buffer length, assumed for EarthCARE to be ~5

532 km, θ_{v} is BBR viewing zenith angle, and $\langle\Delta x\rangle$ is mean length of JSG pixels in the along-track

533   direction. For EarthCARE, $\langle \Delta x \rangle \approx 1$ km. If maximum cloudtop altitude across the entire useable

534   part of the 6,000 km frame is

$$h_F^{\max} = \max\left\{h(i,j)\right\}: i \in \left[m_1 + 1, N_{JSG} - m_2 + 1\right], j \in \left[-m_{assess}, m_{assess}\right], \qquad (19)$$

536   then the absolute maximum number of JSG pixels one need search for outside of $D(n)$ that might

537   obscure part of $D(n)$ is

$$n_{buffer}^{\max} \approx nint\left(\frac{h_F^{\max} \tan\theta_v}{\langle \Delta x \rangle}\right). \qquad (20)$$

539   This can be reduced by knowing the location of the along-track JSG pixel that houses the highest

540   cloud between the last pixel of $D(n)$ and $n_{buffer}^{\max}$ pixels out in front of it. This is expressed as

$$n_{buffer}^{\max}(n) = \underset{i \in \left[n + n_{assess} + n_{buffer}(n),\, n + n_{assess} + n_{buffer}(n) + n_{buffer}^{\max}\right]}{\arg\max}\ h_\perp^{\max}(i). \qquad (21)$$

542   Proceed then to search

$$h_\perp^{\max}(i) \geq \frac{\left[i - (n + n_{assess})\right]\langle \Delta x \rangle}{\tan\theta_v} : i = n + n_{assess} + n_{buffer}, \ldots, n + n_{assess} + n_{buffer}^{\max}(n), \qquad (22)$$

544   where n_{buffer} comes from (18). Let values of i for which the condition in (22) is met form the set

545    $\{i'\}$. Therefore, the size of the buffer-zone for the back-looking view associated with $D(n)$ is

$$n_{buffer}^{\swarrow}(n) = \begin{cases} n_{buffer} & ; \quad \text{if (22) is never met} \\ \max\{i'\} & ; \quad \text{if (22) is met.} \end{cases} \qquad (23)$$

547 To set the size of the buffer-zone for the fore-looking view $n_{buffer}^{\searrow}(n)$, (21) through (23) are reap-

548 plied reversing indices. Figure *4* is a schematic of this process.

549   Note that determination of $n_{buffer}^{\swarrow}(n)$ and $n_{buffer}^{\searrow}(n)$ are independent of θ_0. This is because for

550 EarthCARE's orbit over 80% of observations with $\theta_0 < 90°$ have $30° < \varphi_r < 150°$ implying that,

551 for most cases, projection of direct-beam (and hence cloud shadows) into the along-track ends of

552 $D(n)$ will be small. The exceptions are for very large θ_0 with $150° < \varphi_r < 30°$; but most of these

553 cases will be avoided via the screening process as discussed in section 2.3.2.

554 *b. Across-track length*

555 Next, determine the size of across-track buffer-zones m_{buffer}. They are set using cloud information

556 on the sunlit side of $D(n)$. Here the idea is that if a cloud anywhere to the side of D casts a shadow

557 that falls onto the region formed by D and its along-track buffer-zones, then the across-track buffer-

558 zone extends to include the cloud doing the shadowing. Once m_{buffer} is established, it is applied to

559 the opposing side of $D(n)$, too.

560   Begin by setting a minimum size for the buffer-zone of $d_{\perp}^{min}$, so that searching starts at cross-

561 track JSG pixel $\pm m_{assess} \pm m_{buffer}$, where $m_{buffer} = nint\left(d_{\perp}^{min} / \langle \Delta y \rangle\right)$ is the minimum buffer size in

562 JSG pixels; choice of using $+$ or $-$ depends on which side of D the Sun is on. For EarthCARE,

563 $d_{\perp}^{min} = 5$ km. One then determines the highest cloud in the row of JSG pixels at distance j pixels

564 from L2-plane as

565
$$h_{\parallel}(n,j) = \max\left\{h(i,j)\right\} : i \in \left[n - n_{buffer}^{\swarrow}(n), n + n_{assess} + n_{buffer}^{\searrow}(n)\right].$$
(24)

566 If it happens that

567
$$h_{\parallel}(n,j) \geq \frac{abs(j - m_{assess})\langle \Delta y \rangle}{\tan\theta_0 \sin\varphi_r},$$
(25)

568 is satisfied at j, the across-track buffer gets reset to $m_{buffer} \leftarrow abs(j - m_{assess})$. This process is con-

569 tinued out to the edge of the MSI's swath. *Figure 5* is a schematic of this procedure. The aggrega-

570 tion of an assessment domain D and its buffer-zones is denoted as D^+.

571

References

Barker, H. W. and Z. Li, 1997: Interpreting shortwave albedo-transmittance plots: True or apparent anomalous absorption? *Geophys. Res. Let.*, **24**, 2023-2026.

⸺, M. P. Jerg, T. Wehr, S. Kato, D. Donovan, and R. Hogan, 2011: A 3D Cloud Construction Algorithm for the EarthCARE satellite mission. *Q, J. R. Meteorol. Soc.*, **137**, 1042–1058 DOI:10.1002/qj.824

⸺, S. Kato, and T. Wehr, 2012: Computation of Solar Radiative Fluxes by 1D and 3D Methods using Cloudy Atmospheres Inferred from A-train Satellite Data. *Surveys in Geophys.* **33**, 657-676.

⸺, J. N. S. Cole, and M. Shephard, 2014: Estimation of Errors associated with the EarthCARE 3D Scene Construction Algorithm. *Q. J. R. Meteorol. Soc.*, **140**, 2260–2271, DOI:10.1002/qj.2294.

⸺,⸺, C. Domenech, M. Shephard, C. Sioris, F. Tornow, and T. Wehr, 2015: Assessing the Quality of Active-Passive Satellite Retrievals using Broadband Radiances. *Q. J. R. Meteorol. Soc.*, **141**, 1294–1305, DOI:10.1002/qj.2438.

⸺, P. M. Gabriel, Z. Qu, and S. Kato, 2021: Representativity of Cloud-Profiling Radar Observations for Data Assimilation in Numerical Weather Prediction. *Q. J. R. Meteorol. Soc.*, **147**, 1801–1822. https://doi.org/10.1002/qj.3996.

⸺, J. N. S. Cole, Z. Qu, N. Villefranque, and M. W. Shephard, 2023: Radiative Closure Assessment of Retrieved Cloud and Aerosol Properties for the EarthCARE Mission: The ACMB-DF Product. *Atmos. Meas. Tech.*, to be submitted.

Cole, J. N. S, H. W. Barker, Z. Qu, N. Villefranque, and M. W. Shephard, 2023: Broadband Radiative Quantities for the EarthCARE Mission: The ACM-COM and ACM-RT Products. *Atmos. Meas. Tech.*, to be submitted.

Donovan, D. P., P. Kollias, and G-J van Zadelhoff, 2023: The Generation of EarthCARE L1 Test Data sets Using Atmospheric Model Data Sets. *Atmos. Meas. Tech.*, to be submitted

Eisinger, M., T. Wehr, T., Kubota, D., Bernaerts, and K. Wallace, 2023: The EarthCARE production model and auxiliary products. *Atmospheric Measurement Techniques*, to be submitted.

ESA., 2001: *The Five Candidate Earth Explorer Missions: EarthCARE –Earth Clouds, Aerosols and Radiation Explorer,* ESA SP-1257(1), September 2001. ESA Publications Division: Noordwijk, The Netherlands.

Illingworth, A. + others, 2015: THE EARTHCARE SATELLITE: The next step forward in global measurements of clouds, aerosols, precipitation and radiation. *Bull. Am. Met. Soc.*, **96**, 1311-1332. DOI:10.1175/BAMS-D-12-00227.1.

⸺ + others, 2018: WIVERN: A New Satellite Concept to Provide Global In-Cloud Winds, Precipitation, and Cloud Properties. *Bull. Am. Met. Soc.*, **99**, 1669–1687. https://doi.org/10.1175/BAMS-D-16-0047.1

606 Marshak, A., A. Davis, W. Wiscombe, W. Ridgeway, R. Cahalan, 1998: Biases in Shortwave Column Ab-
607   sorption in the Presence of Fractal Clouds. *J. Climate*, **11**, 431-446.

608 Platnick, S., Ackerman, S., King, M., et al., 2015: MODIS Atmosphere L2 Cloud Product (06_L2). NASA
609   MODIS   Adaptive   Processing   System,   Goddard   Space   Flight   Center,   USA:
610   http://dx.doi.org/10.5067/MODIS/MOD06_L2.006.

611 Qu, Z., D. P. Donovan, H. W. Barker, Cole, J. N. S, M. W. Shephard, and V. Huijnen, 2023: Numerical
612   Model Generation of Test Frames for Pre-launch Studies of EarthCARE's Retrieval Algorithms and
613   Data Management System. *Atmos. Meas. Tech.*, to be submitted

614 Sun, X. J., H. R. Lia, H. W. Barker, R. W. Zhang, Y. B. Zhou and L. Liu, 2016:Estimation of cloud base
615   heights based on the matching of multiple cloud characteristics. *Q. J. R. Meteorol. Soc.*, **142**, 224-
616   232, DOI:10.1002/qj.2647.

617 Tornow, F., H. W. Barker, and C. Domenech, 2015: On the use of Simulated Photon Paths to Co-register
618   TOA radiances in EarthCARE Radiative Closure Experiments. *Q. J. R. Meteorol. Soc.*, **141**, 3239-
619   3251. DOI:10.1002/qj.2606.

620 USGS Earth Resources Observation and Science (EROS) Center, 2018: USGS EROS Archive - Land Cover
621   Products - Global Land Cover Characterization (GLCC) Background, https://www.usgs.gov/cen-
622   ters/eros/science/usgs-eros-archive-land-cover-products-global-land-cover-characterization-0#over-
623   view (last access: April 5, 2022).

624 van Zadelhoff, G.-J., H. W., Barker, E., Baudrez, S., Bley, N., Clerbaux, J. N. S., Cole, J., de Kloe, N.,
625   Docter, C., Domenech, D. P., Donovan, J.-L. Dufresne, M., Eisinger, J., Fischer, R., García-Marañón,
626   M., Haarig, R. J., Hogan, A., Hünerbein, P., Kollias, R., Koopman, T., Wehr, 2022: EarthCARE level-
627   2   demonstration   products   from   simulated   scenes   (09.01)   [Data   set].   Zenodo.
628   https://doi.org/10.5281/zenodo.7117116

629 Velázquez-Blázquez, A., E. Baudrez, N., Clerbaux, C., Domenech, R. G., Marañón, and N. Madenach,
630   2023: Towards instantaneous top-of-atmosphere fluxes from EarthCARE: The BMA-FLX product.
631   *Atmospheric Measurement Techniques*, to be submitted.

632

633